Mon. Not. R. Astron. Soc. **000**, 1–20 (2015) Printed 28 July 2015 (MN LATEX style file v2.2)

Molecular cloud formation in high-shear, magnetized colliding flows

E. L. Fogerty[1⋆], A. Frank[1], F. Heitsch[2], J. Carroll-Nellenback[1], C. Haig[2] and M. B. Adams[1]

[1] *206 Bausch & Lomb Hall, Department of Physics & Astronomy, University of Rochester, Rochester, New York, 14627, United States*
[2] *3255 Phillips Hall, Department of Physics & Astronomy, University of North Carolina, Chapel Hill, North Carolina, 27599, United States*

Submitted 2015 February 28

ABSTRACT

Recent evidence suggests that star formation occurs during or shortly after the formation of molecular clouds. Under this assumption, models of molecular cloud formation should provide mechanisms capable of driving rapid fragmentation of the gas into stars. Models of large-scale colliding flows have identified such mechanisms. Previously, we have explored hydrodynamical simulations of colliding flows to study morphology, dynamics, and protocluster formation within the collision zone (Carroll-Nellenback, Frank & Heitsch 2014). Here, we extend these simulations by exploring the effect of adding a weak magnetic field to the flows and shear at the collision interface. Shear is generated in our simulations by varying the inclination of the collision interface. We find that the initial conditions in magnetized shear flows can become erased, as evidenced by the reallignment of a highly oblique collision interface. We also find that magnetic fields and shear greatly impede gravitational collapse.

Key words: *magnetohydrodynamics* (MHD) – ISM: evolution – ISM: structure – stars: formation – methods: numerical.

1 INTRODUCTION

The interstellar medium (ISM) is a dynamic and ever changing environment. It exists in various thermal states, appearing to continuously cycle from a warm, sparse phase to a cold, dense phase and back again. The evolution of the gas through these phases paints a picture of star formation, one in which star-forming molecular clouds are not long-lived, steady state structures as once believed. Rather, they are transient structures born out of the cold, dense phase of the ISM.

Many well known lines of evidence support the notion of transient molecular clouds, and thus the basis of todays star formation theory: i) there is a dearth of starless clouds, ii) most of the stars in clouds are under the age of 5 Myr, and iii) there is a high degree of hierarchical structure present in molecular clouds that would simply not last long due to star-star scattering or tidal interactions (Elmegreen 2000; Hartmann 2001; Ballesteros-Paredes & Hartmann 2007). Indeed, this idea of short cloud lifetimes and its connection to fast star formation is not new. Connections to this idea can be found in work that dates back now at least several decades (Hunter 1979; Larson 1981; Hunter et al. 1986). Given the complexity that comes with a dynamical theory of molecular cloud evolution, however, it was only possible to test with modern computational methods.

One well known mechanism for generating transient, structured molecular clouds is the collision of two large-scale streams of gas - a scenario called the 'colliding flows' model. Simulations of colliding flows show that nonlinear density structures can easily form in the shocked collision region between the flows via various instabilities (cf. Heitsch et al. (2005) for a quick discussion of the instabilities). Further, these structures become dense enough over long enough timescales to allow for H_2 formation, becoming effectively 'molecular'. Gravitational instabilities cause the turbulent, shocked gas to collapse and form stars (i.e. sink particles). Given the highly dynamical environment, the whole process from molecular cloud formation to star formation to cloud destruction occurs in roughly a dynamical time, agreeing well with observations (Audit & Hennebelle 2005; Heitsch et al. 2006; Vázquez-Semadeni et al. 2006; Heitsch et al. 2008).

While these models are highly idealized, they are not without motivation. Coherent large-scale streams of gas are plausible in many situations in the ISM: expanding bub-

⋆ E-mail:erica@pas.rochester.edu

© 2015 RAS

bles driven outward from energetic OB associations and/or supernovae, turbulent motions arising from gravitational instabilities, density waves in the spiral arms of galaxies, and cloud-cloud collisions have all been proposed as potential drivers (Hartmann, Ballesteros-Paredes & E. 2001; Inutsuka et al. 2015). In fact, there has been a growing body of observational support for the colliding flows picture. Looney et al. (2006) demonstrates an active star forming molecular cloud core likely arose from cloud-cloud collisions. Atomic inflows surrounding molecular gas have been observed in Taurus (Ballesteros-Paredes, Hartmann & Vázquez-Semadeni 1999) and other molecular clouds (Brunt 2003). Molecular clouds have been found at the edges of supershells (Dawson et al. 2011, 2013).

In addition to these findings, there has been a recent surge of magnetic field measurements in relation to molecular cloud complexes, and the ISM in general (Beck (2001); Alves, Franco & Girart (2008); Sugitani et al. (2011); Palmeirim et al. (2013) and references therein). Polarization maps in these studies suggest allignment of the magnetic field with molecular clouds. Further, gas seems to be accreted onto the clouds along the magnetic field lines. While this alone underscores the importance of adding magnetic fields to models of molecular cloud formation, additional motivation comes from work that links colliding flows to these features. For instance, Peretto et al. (2012) demonstrate the morphology and respective magnetic field orientation of the pipe nebula likely arose from large-scale compressions.

Depending on the dynamical strength of the magnetic field, various features of ISM/molecular cloud dynamics have been established from colliding flows simulations. On the largest scales, the important turbulent generating instabilties like kelvin helmoltz (KH) and the nonlinear thin-shell instability (NTSI) can be suppressed (Heitsch et al. 2007), leading to a lesser degree of turbulent substructure in the forming clouds (Hennebelle et al. 2008). On smaller scales, i.e. scales of clouds and cores, gravitational collapse can be slowed and the observed power law relation between the magnetic field strength and density ($B \propto n^k$, for $1/2 < k < 2/3$, Troland & Heiles (1986); Crutcher (1999); Crutcher et al. (2010); Tritsis et al. (2015)) can be reproduced (Hennebelle et al. 2008; Banerjee et al. 2009; Heitsch, Stone & Hartmann 2009; Vázquez-Semadeni et al. 2011).

While the colliding flows model has produced a wealth of knowledge into molecular cloud formation, all of the simulations mentioned here studied the flows intersecting at a normal shock interface. It is thus worthwhile to explore the consquences of varying the obliquity of the collision interface. Such oblique shocks can arise in all of the motivating situations described above. It is in fact easy to imagine, as a direct head-on collision is highly contrived. As the flows would enter the oblique shocks created at the interface, a strong shear velocity field would result, giving rise to the question - how does added shear affect cloud and star formation?

Recently, Körtgen & Banerjee (2015) looked at varying the intersection of magnetized colliding flows to mimic the effect of magnetic diffusion. There, the magnetic field was kept parallel with one flow, while the other flow was inclined with respect to the first. This high shear environment delayed star (i.e. sink particle) formation, as well as the star formation efficiency of the gas. Körtgen & Banerjee (2015) attribute this to the high shear breaking up dense structures, and thus impededing gravitational instability.

With a slightly different focus, we study how varying the angle of the collision interface alone affects the bulk dynamics of the flow. We perform a set of 4 simulations, varying the collision interface from a normal incidence to highly inclined. All of our simulations include a uniform magnetic field aligned with the flows to simulate idealized ISM conditions, in addition to self gravity and cooling. We present our numerical model in Section 2, our results in Sections 4-8, and our summary in Section 9.

2 NUMERICAL MODEL

We ran 3-dimensional colliding flows simulations using Astrobear[1] (Carroll-Nellenback et al. 2013). Astrobear is a free to download, massively parallelized, adaptive mesh refinement (AMR) code that is suitable for a wide-range of astrophysical contexts. It contains many preloaded multiphysics solvers, such as, self-gravity, magnetic resistivity, radiative transport, etc.

The setup consisted of two, 40-pc diameter cylinders colliding in a 3D box under the influence of gravity, magnetic fields, and cooling. The ideal magnetohydrodynamic (MHD) equations including gravity and cooling source terms were solved using a Strang-split corner upwind transport (CTU) scheme that was 2nd-order accurate in time combined with a directionally unsplit CTU scheme for the hydro steps. For the hyperbolic steps, we used the Harten-Lax-van Leer with Discontinuities (HLLD) Reimann solver. Gravitational interactions included both the self-gravity of the gas, as well as the gravitational acceleration due to sink particles, which were implemented following Federrath et al. (2010). To solve Poisson's equation for the gravitational potential of the grid, Astrobear uses the external package, **HYPRE**[2] (Falgout & Yang (2002), cf. Kaminski et al. (2014) Appendix for a description of Astrobear's self gravity algorithm). The magnetic field was initalized to be uniform and parallel to the flows at a strength of $B = 1.3\ \mu G$. This field strength is within reason of current ISM magnetic field estimates (Beck 2001; **?**). Given the setup of the simulations, the field was dynamically weak, with $\beta_{plasma}(t = 0) = 10$ and $\beta_{ram}(t = 0) \approx 38$ inside of the flows ($\beta_{plasma(ram)}$ is the ratio of thermal (ram) pressure to magnetic pressure). Cooling processes in the box followed a parameterized cooling curve adapted from **?** to include the effects of UV shielding. This modification allowed the gas to cool to $T = 10\ K$ for densities greater than $n > 1000\ cm^{-3}$ (Ryan & Heitsch in prep).

Sink particles formed in our simulations only after a series of checks had been satisfied, e.g.,

(i) a cell and surrounding region was Jeans unstable
(ii) the center cell (i.e. location of potential sink) in this Jeans unstable region was collocated with a gravitational potential minimum

[1] https://astrobear.pas.rochester.edu/trac/
[2] HYPRE is a software package that solves linear systems on massively parallelized systems. Documentation on Hypre can be found at: https://computation.llnl.gov/casc/hypre/software.html

Table 1. The suite of simulations. The inclination angle (see text) is denoted by θ, L_x, L_y, and L_z denote the box dimensions, and t_{sim} is the final simulation time. Note the box size was increased in x to accomodate steeper inclination angles

θ (°)	L_x (pc)	$L_y,\ L_z$ (pc)	$t_{sim}(Myr)$
0	62.5	75	27.3
15	62.5	75	27.3
30	200	75	27.3
60	200	75	32.8

(iii) the surrounding region was exhibiting a converging flow into this center zone

etc., as given in Federrath et al. (2010). These checks ensure that sinks form only when appropriate, i.e. when a region would go on to form a gravitationally bound object such as a protostar, if better resolution were available. Given the size of our finest cell ($\Delta x_{min} = 0.05\ pc$), we identify single sink particles as proto*clusters* rather than protostars. Thus, we will use the words 'sink' and 'protocluster' interchangeably.

Sink particles that form interact with the gas (and other sinks) around them, just as a physical, self-gravitating object in the grid would – i.e. through gravitational interactions and the ability to accrete surrounding material. They remain individual objects throughout the course of the simulation (i.e. do not merge), and do not provide any form of energy or momentum feedback into the surrounding medium. Gas around a sink particle is accreted only when the density in the surrounding zones exceeds a given threshold, dictated by the Truelove criterion (cite), and then only the excess gas is removed from those cells (cite). In this way, material is not always taken away from the surrounding zones, but rather only when the surrounding zones themselves are undergoing gravitational collapse.

The suite of simulations consisted of four runs, each with a different orientation of the collision interface, specified by the inclination angle θ (Fig. 1). The inclination angle varied between $\theta = 0°$, representing a head-on collision, to $\theta = 60°$, i.e. a highly inclined collision. In previous work, Carroll-Nellenback, Frank & Heitsch (2014) explored hydrodynamical simulations of a head-on collision between two 40-pc diameter flows. All parameters for the present suite of runs are the same as in Carroll-Nellenback, Frank & Heitsch (2014), with the exception of the magnetic field, and variation of the collision interface. This allowed us to compare our head-on case to the 'smooth' colliding flow in Carroll-Nellenback, Frank & Heitsch (2014), and thus explore the effects of adding a magnetic field, in addition to studying the effects of shear. For this reason, we will refer to the smooth colliding flow in Carroll-Nellenback, Frank & Heitsch (2014) as 'the hydro run' here. To accommodate steeper inclination angles, we increased the box size in the x dimension from $L_x = 62.5$ to $L_x = 200\ pc$ in the $\theta = 30$ and 60° runs (Table 1). Note, this is because θ measures down from the positive $\hat{z}$-axis, in the x-z plane, as can be seen in Fig. 1. Three of the runs ($\theta = 0$, 15, and 30°) had the same final run time of $t_{sim} \approx 27\ Myr$. The $\theta = 60°$ did not form any sink particles by this time, and so was extended until $t_{sim} \approx 33\ Myr$.

The flows were injected into a stationary ambient medium at a velocity of $v = 11\ km\ s^{-1}$ and an isothermal

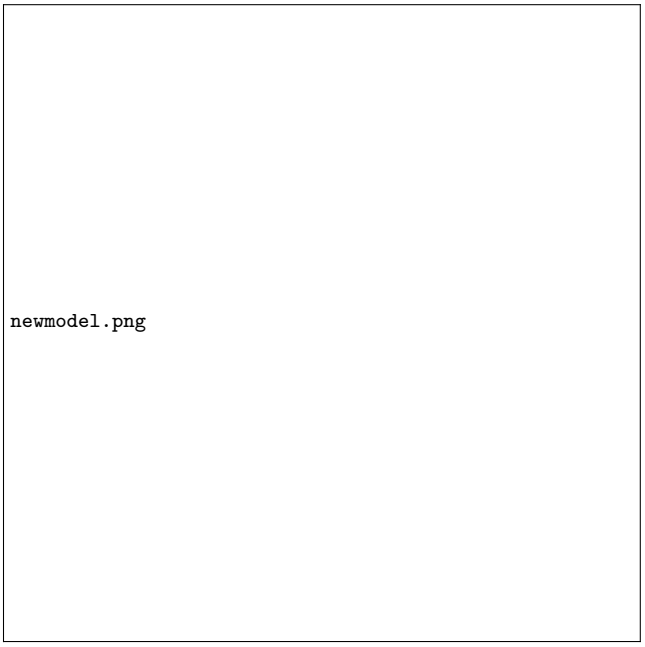

Figure 1. Model of flows. The colored cylinders represent the two oppositely driven flows that were aligned along the $\hat{x}$-axis, the straight-lines indicate the initial magnetic field geometry, and the inclination angle θ measures the rotation of the collision interface about the $\hat{y}$-axis.

mach of $M = 1.5$. All gas in the box had a mean molecular weight of $\mu = 1.27$, making the gas effectively atomic hydrogen. We used an ideal gas equation of state with $\gamma = 5/3$. The gas was initially in thermal equilibrium at a uniform number density of $n = 1\ cm^{-3}$, corresponding to the stable warm nuclear medium (WNM) phase of the cooling curve. This set the thermal pressure and temperature everywhere inside the box to be $P_{therm}\ k_B^{-1} = 4931\ K\ cm^{-3}$, and $T = 4931\ K$, where k_B is the Boltzmann constant. The ram pressure of the flows was $P_{ram} k_B^{-1} = 18,500\ K\ cm^{-3}$, giving a mass flux into the collision region of $M_{flux} \approx 886\ M_\odot Myr^{-1}$.

As in previous simulations, the collision interface was seeded with a set of random sinusoidal velocity perturbations to excite the NTSI and KH instabilities (cf. Heitsch et al. (2006), Carroll-Nellenback, Frank & Heitsch (2014)). These perturbations had a maximum amplitude of $A = 2\ pc$, spectral index $\alpha = -2.0$, and maximum wavenumber $k_{max} = 16$. Boundary conditions on the box were set to inflow-only on the faces where the flows were injected, and extrapolating on all other faces. The boundary conditions for the gravity solver were multipole expansion.

Our analysis will focus mainly on the $\theta = 0$, 15, and 60° cases, as the $\theta = 30°$ case did not differ significantly from the $\theta = 15°$ case.

3 MASS-TO-FLUX RATIO

Following Vázquez-Semadeni et al. (2011), the critical mass-to-flux ratio (m2fr) of cylindrical uniform flows (in terms of the initial magnetic field strength B, and the mass column

density $\Sigma = \rho L$, where ρ is the mass density and L is the column length) is given by (cite Nakamura and Nakano '78),

$$\mu_{crit} = \frac{\Sigma}{B} \approx \frac{1}{\sqrt{4\pi^2 G}} \quad (1)$$

This can be recast in terms of a critical length scale for values relevant to the ISM (cite Hartmann 2001),

$$L_{crit} \approx 470\ (\frac{B}{5\ \mu G})(\frac{n}{cm^{-3}})^{-1}\ pc \quad (2)$$

This last equation describes the *accumulation length* of a cylindrical flux tube, i.e. the length at which enough mass has been accumulated to become magnetically supercritical (for a cylinder of number density n and threaded by parallel magnetic field B). For our initial values, this equation gives the critical length as $L_{crit} \approx 122\ pc$. This means that for two of our runs ($\theta = 0$ and $15°$), the length of the cylinder is not long enough to contain enough mass to render it magnetically supercritical. In the bigger box cases ($\theta = 30$ and $60°$), however, the length of the cylinder exceeds the critical length and so in those cases the flows start magnetically supercritical.

For the case of the initially subcritical flows, one can solve for the time it takes the cylinder to become supercritical, given the mass flux into the box. For this, it is helpful to recast Equation (1) in terms of the critical column number density. Conveniently given in terms of ISM values this is (cite),

$$N_{crit} \approx 1.45 \times 10^{21} \frac{B}{5\mu G}\ cm^{-2} \quad (3)$$

Equating Eqn. (3) to the time-dependant column number density of a cylinder of initial mass (M_0) and area (A),

$$N(t) = \frac{M_0 + \dot{M}t}{\mu m_H A} \quad (4)$$

and solving for t, yields a timescale to go unstable,

$$t_{crit} = \frac{1}{\dot{M}}(1.45 \times 10^{21}(\frac{B}{5\mu G})(\frac{A\mu m_H}{cm^2}) - M_0) \quad (5)$$

This equation gives the timescale for the entire cylinder (i.e. the two flows combined) to go unstable as $t \approx 2.6\ Myr$. Thus, while the $\theta = 0$ and $15°$ start out magnetically subcritical, they quickly (i.e. $t_{crit} << t_{sim}$) acquire enough mass to become supercritical. We therefore do not expect to see large differences attributed to the difference in criticality of the flows.

On smaller scales, one can predict the timescale for just the collision region to go unstable. Considering the collision region to be thin (initially massless), the column density of just the collision region can be approximated as,

$$N(t) = 2nvt \quad (6)$$

where v is the speed of the flows. Equating this to Eqn. (3) and solving for t gives the following timescale to go unstable in terms of ISM relevant parameters (cite Heitsch),

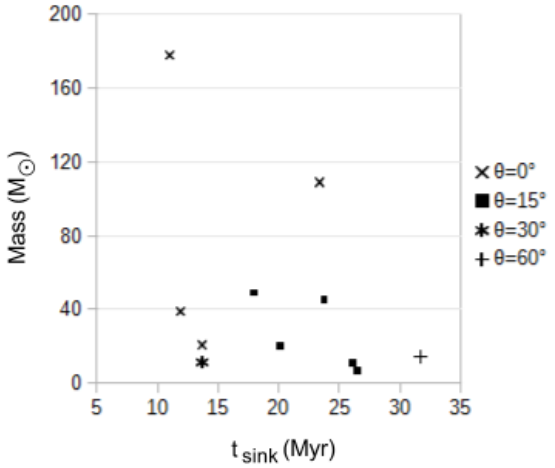

Figure 2. Final mass distribution of protoclusters as a function of formation time, t_{sink}. With increasing shear angle, it takes longer to form protoclusters and the total protocluster mass declines. Note, the final simulation time was the same for the $\theta = 0$ and $\theta = 15°$ ($t_{sim} = 27.3\ Myr$), but was longer for the $\theta = 60°$ case ($t_{sim} = 32.8$). Also, mass accretion is not constant over time, but rather dependant on environmental conditions (see text).

$$t_{crit} \approx 5.65(\frac{B}{5\mu G})(\frac{n}{cm^{-3}})^{-1}(\frac{v}{10\ km\ s^{-1}})^{-1}\ Myr \quad (7)$$

Thus, in *all* of our simulations the collision region itself is predicted to go unstable within $t \approx 1.3\ Myr$, due to the self-gravity of the collision region overtaking the supportive strength of the magnetic field.

As Vazquez (2011) discusses, the timescale to become magnetically supercritical is comparable to the timescale of the gas to become molecular *and* self-gravitating. Thus, it is easy to expect the gas to quickly evolve into a supercritical, molecular state. However, it is important to note that the m2fr is actually a highly varying quantity within the collision zone (cite Vazquez), and there are other forms of support not taken into account that can withstand collapse, as we will show.

4 PROTOCLUSTER FORMATION AND EVOLUTION

The effect of shear is readily apparent considering protocluster formation in the various runs. As can be seen from Fig. 2, protocluster formation declined with increasing inclination angle. This is evident both by the decreasing number of protoclusters, as well as the increasing latency of protocluster formation with increasing inclination angle. The steepest inclination angle case ($\theta = 60°$) was so inhospitable to protocluster formation that it did not form *any* protoclusters in the final run time of the other simulations. Only after extending the $\theta = 60°$ case out another 5 Myr did a protocluster eventually form ($t_{sink}(\theta = 60°) \approx 32\ Myr$).

The overall weaker protocluster formation in high shear environments is understandable by considering Eqn. 7 - the timescale to acquire enough material into the central region

to go magnetically supercritical. As the inclination angle varies, the velocity in Eqn. 7 becomes $v' = v\cos\theta$, due to deflection at the collision interface (i.e. the generation of shear). Thus, the critical timescale for shear environments is related to Eqn. 7 by,

$$t'_{crit} \propto t_{crit}(\cos\theta)^{-1} \quad (8)$$

This equation predicts longer timescales to go unstable in higher shear environments, consistent with the increased time to form protoclusters and the overall reduction in protocluster number.

Since the protoclusters are not all forming at the same time, the anti-correlation between final masses and inclination angle apparent in Fig. 2 somewhat depends on the amount of time each protocluster has to accrete. However, not in all cases. For instance, the $\theta = 30^\circ$ case. While appearing to be an outlier in the above argument by forming a protocluster before the $\theta = 15^\circ$ case, the 30° case is extremely low-mass despite having ample time to grow. This indicates that while the msfr must have been supercritical in the region where the protocluster formed, it did not remain so for very long. Strong shearing motions in this case prevented the further growth of the protocluster.

To compare the mass distribution across runs, it is imperative to normalize them. One way to do this is to compare protoclusters from different simulations that are roughly coeval. This shows protoclusters that form in lower shear cases can accrete mass faster than their higher shear counterparts. The strongest example of this are the two protoclusters that formed at $t \approx 24\ Myr$, where the $\theta = 0^\circ$ protocluster grew to be $\approx 3\times$ more massive than its $\theta = 15^\circ$ counterpart. While this trend holds for both coeval pairs that are less than 5 Myr apart, given the small number of protoclusters formed, such statistics are not strongly conclusive. Thus, we can say at best there is a weak anti-correlation between final protocluster mass and inclination angle.

Finally, there is a stark reduction in the number of protoclusters formed in the $\theta = 0^\circ$ case compared to the hydro version of this run in Carroll-Nellenback, Frank & Heitsch (2014). For the same final simulation time and resolution, the hydro run formed a total of 25 protoclusters compared to the 4 formed in the $\theta = 0^\circ$ case. This clearly shows the great support magnetic fields can provide against collapse. Comparing the final masses overall of the MHD shear runs to the hydro run shows that in total, the final masses of the MHD shear protoclusters were similar in distribution to the hydro run, around $M = 100\ M_\odot$ or less. As discussed in Carroll-Nellenback, Frank & Heitsch (2014), this, combined with their formation positions being off-center from the global gravitational potential well (as seen in column density maps, presented in Section 5), suggests that collapse was due to local fragmentation, rather than global collapse.

5 MORPHOLOGY - COLUMN DENSITY MAPS

5.1 $\theta = 0^\circ$ case

Column density maps for the different runs are of the whole domain along a given perspective. Because of this, they include undesirable artifacts from the model, such as ejecta from the collision region (expelled due to the imbalance in pressures between the collision region and surrounding ambient medium). In the case of MHD runs, this also includes a large ring-like structure (cite), present at $r \approx 30\ pc$ from the center of the collision region in the $\theta = 0^\circ$ case (Fig. 3, left). This artifact is created when material expelled from the collision region collides with the ambient magnetic field, distorting the field lines and thus creating regions of high magnetic tension. At some radius, this magnetic tension becomes strong enough to counteract any further bending of the field lines, thereby halting and collecting ejecta. A simple model describing this process predicts the position of this ring. Let,

Equations here.

Because this ring is an artifact of the model, we will limit this discussion to column density structures that form within the 40 pc diameter collision region.

Structures within the collision zone of the $\theta = 0^\circ$ case (Fig. 3) are morphologically similar to the hydro analog of these runs (Carroll-Nellenback, Frank & Heitsch (2014), fig. 2), with perhaps an overall less knotty appearance, similar to what (cite Vazquez) report. That is, larger, coherent filamentary structures are present in the MHD case that resemble clouds (cite).

As can be seen in the CDM, the column densities become great enough by t - x for these filamentary clouds to become molecular (cite),

and self-gravitating (cite),

However, without plotting the m2fr one is left to gauge regions of supercriticality by the positions of the sink particles.

The clouds that form are high enough in density to become molecular starting at t - 10 Myr and present until 30 Myr where stars start to form. (cite equation to go molecular). The densities do not reach high enough to warrant ambipolar diffusion (cite Heitch).

In addition to this ring of dense material around the collision region, the flows appear less knotty and localized in the MHD case than in the hydro run. The gas rather accumulates in larger islands, visible in both perspectives of the column density maps.

This is due to the gas being tied to the field lines, unable to cross them. The gas builds up in the yz plane and along the flow dimension until enough gathers so that gravitational collapse can proceed (cite). Indeed this explains the stark difference in the number of protoclusters formed in the MHD case – it takes longer to go untsable in the MHD case, given the lateral support of gas due to the field.

Eventually, the weight of the gas overwhelmed the supportive forces present within the gas and protoclusters formed, the first of which are visible in the CDM by $t = 20\ Myr$. Zooming in on the image shows that they are all 3 clustered together in the upper right of the flow in the left panel of the figure, indicating that they did not form in the global potential minimum of the flows. These protoclusters formed in a small spherical volume of $r = .25\ pc$; the production of 3 protoclusters in such a small region shows the greater gravitational instability of the surrounding environment.

In the last time panel of the CDM, another protocluster has formed roughly $r = 25\ pc$ away. This position also

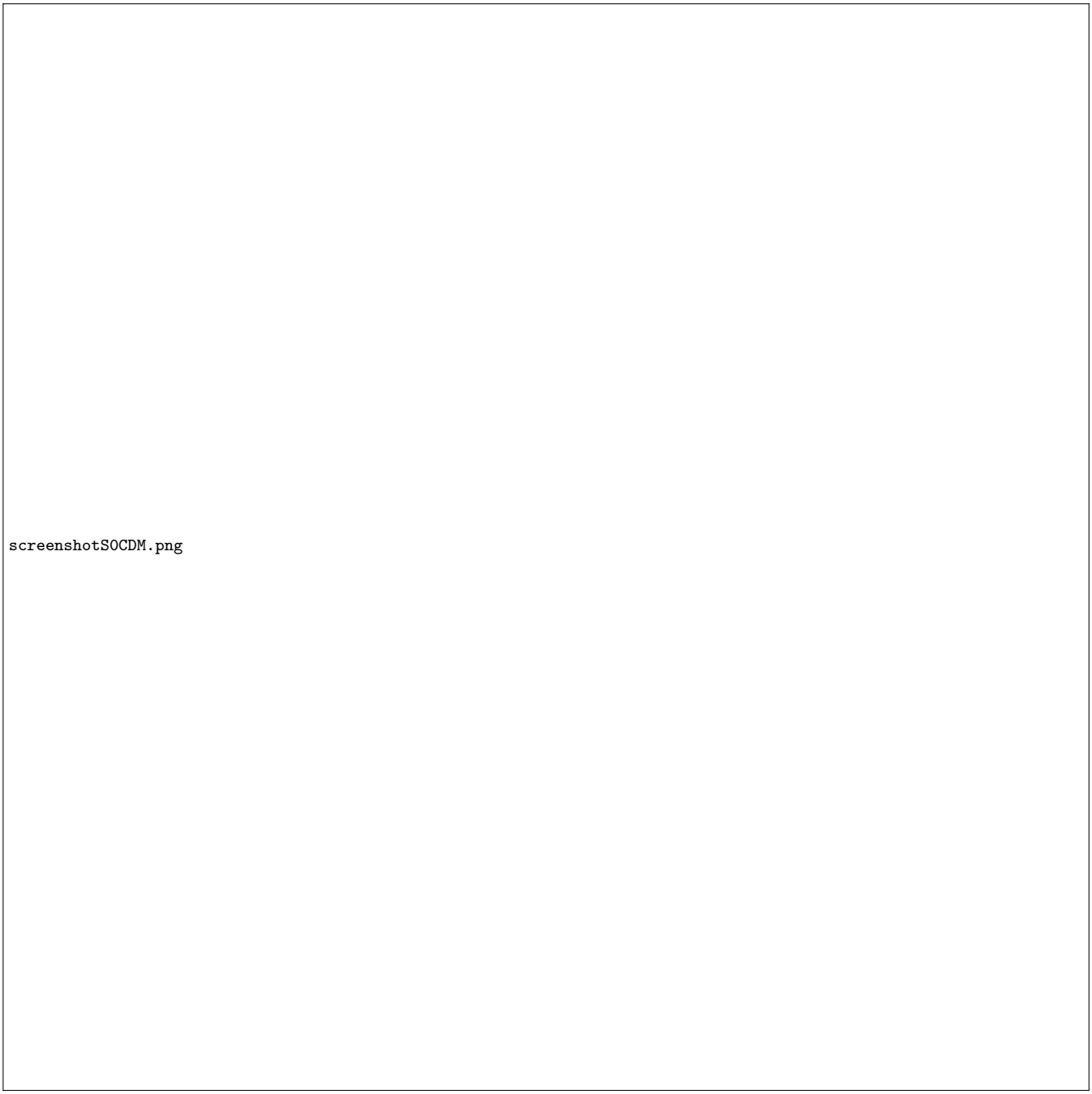

Figure 3. CDM, Shear 0

was off-center when viewed in the 2 different projections, but was within a a rather large island of high density material. A quick check at Fig. 2 shows that this protocluster had the fastest average accretion rate of all the $\theta = 0^{\circ}$ protoclusters, indicating the strong gravitational instability in its surrounding vicinity.

5.2 θ= 15° case

The CDM of the $\theta = 15^{\circ}$ case is morphologically similar to the $\theta = 0^{\circ}$ case at $t = 10\ Myr$, in the yz-plane. Looking in the xz-plane at this same time, shows the slight tilt of the collision interface of this run. By $t = 20\ Myr$, the first protocluster has formed, shown in the center of the CDM in the left-hand panel, and in one of the nodes of the non-linear thin shell instability (NTSI) in the right-hand panel. Over time, the fingers of the NTSI grow, and by $t = 27.3\ Myr$, the instability has become 'z-shaped', with a large component aligned to the flow axis, and 2 shorter arms jutting through vertically. Four additional protoclusters have formed in the flows by this time. Two of them were in the same NTSI node as mentioned above, and 2 others were approximately $r \approx 10.2$ and 21.9 pc away, near the edge of the cylinder.

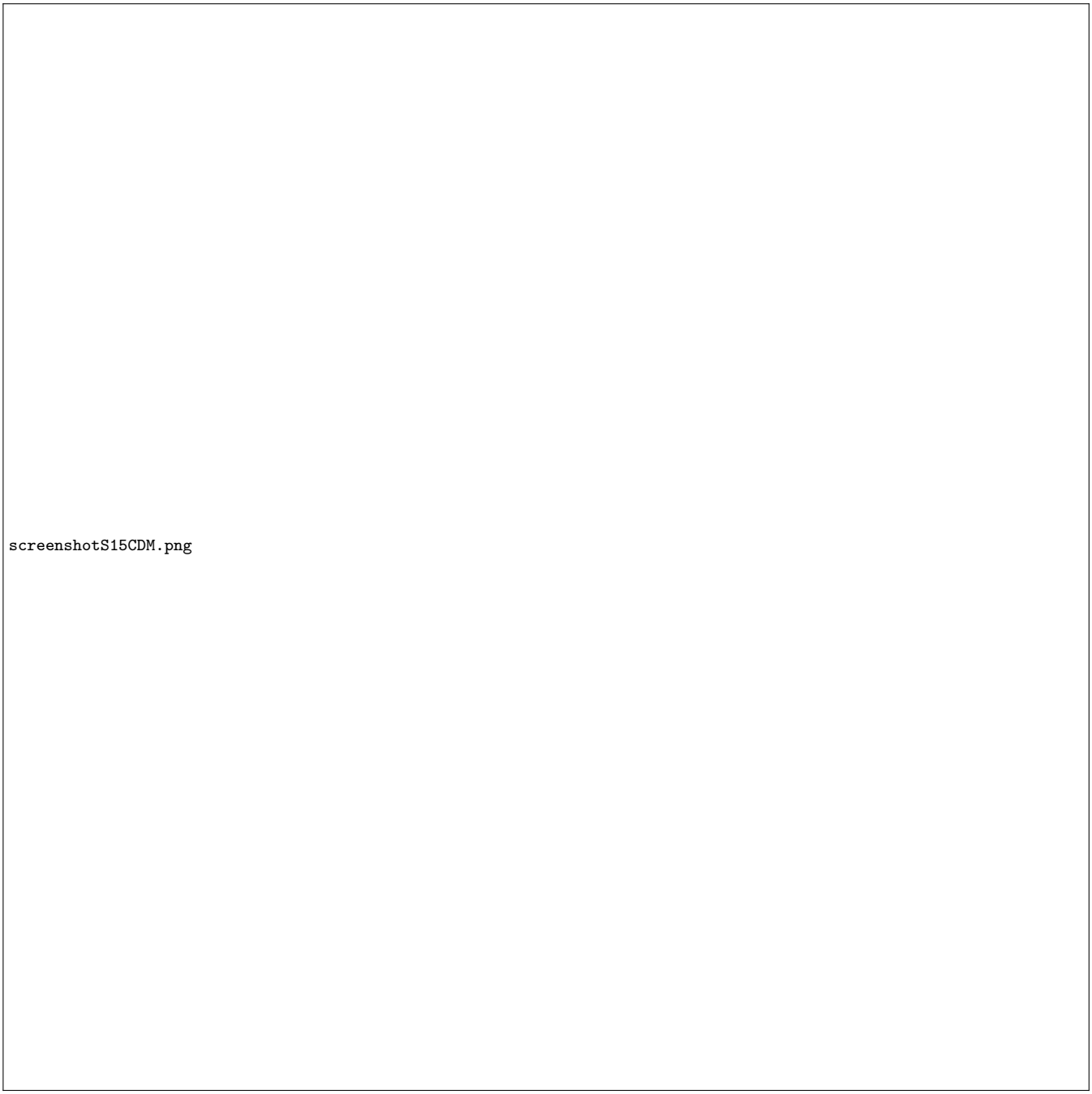

Figure 4. CDM of Shear 15

5.3 θ= 60° case

The $\theta = 60°$ case exhibited very different behavior than the previous 2 runs: the original steep angle of the collision interface reoriented over time, such that it approached the $\theta = 0°$ case. (Can we identify any features in the spectra on large scale that explains this reorientation? How does this compare to other authors/work?). We envision this process as happening as follows. The perturbations at the collision interface seed the NTSI. Given the orientation of the interface with respect to the incoming flow, this NTSI must have some 'vertical' component when seen in the xz plane. This it does, as can be seen in the right panel of Fig. 5, at $t = 10.1\ Myr$. As the flow continues into the collision region it meets this vertical component of this NTSI 'node', which acts like a wall to the incoming flow. Thus incoming material is deflected away vertically from this region. This material cannot travel unimpeded by the magnetic field, and begins to collect in troughs above and below the vertical band, as seen by $t = 20.1\ Myr$ (Fig. 5, right). Over time, this process continues to build an ever larger vertical wall, so that the original tilted angle of this case is erased by $t = 27.3\ Myr$, and what is left is a collision interface that resembles the $\theta = 0°$ run. By $t = 32.8\ Myr$ the lack of steep shear enables gravitational collapse to set-in, and a sole protocluster

is evident on the CDMs, forming about mid-way along the collision region in the xz-plane, but off-center in the yz-plane (Fig. 5, left, last panel).

It is also interesting to note that looking down-the-barrel of the flows (Fig. 5, left) at $t = 10.1\ Myr$ shows the collision region was less dense than the other runs at this time, and this is due to the large shear being generated by the steep tilt of the collision region; incoming material was sharply deflected away from the center of the cylinder making for less accumulation of material in this region early on. This is also notable in the perpendicular perspective at the same time (Fig. 5, right) – the collision interface is thin compared to the other 2 runs, and this is because material is deflected away from the region rather than penetrating it and piling up along the flow axis. By $t = 20\ Myr$, given the growth of the vertical bar as discussed above, material begins to accumulate in the collision region (Fig. 5, left), and continues to do so over the next two time panels, until local collapse has set-in and a protocluster has formed.

6 THERMODYNAMICS - COLUMN β^{-1} MAPS

Column maps of β^{-1}, showing the relative strength of the magnetic pressure to the thermal pressure in the flows, are presented in this section. These maps were made by integrating β^{-1} along a given dimension, and therefore represent the average β^{-1} looking down a given perspective. Sink particles are plotted on top of these maps as in Section 5, but now are given as black points.

6.1 $\theta = 0^\circ$ case

As discussed above, splashing from the collision region deforms the magnetic field which should leave a signature in column β maps. In the head-on case this would be most prominent as a ring of high β^{-1} material coinciding with the ring of high n material discussed in Section 5. This is what we see. Looking in the left-hand panel of Fig. 6 at $t = 10.1\ Myr$ shows the field is being amplified at a distance of $r \approx 30\ pc$ from the center of the collision region, with β^{-1} increasing 10-fold in peak regions from its initial value of 0.1. This ring is knotty in appearance just as it was in column density, showing that an increase in β^{-1} is correlated with the formation of dense structures as well as the large-scale deformation of the field due to splashing.

Additionally, there is another, inner ring that is present from $t = 10.1\ Myr$ on at a distance $r \approx 15\ pc$ from the center of the colliding flows that is not present in the column density maps (why). This ring is not contained in the collision region itself, as can be seen from the perpendicular perspective (right-hand side, Fig. 6), but rather, stretches down the cylinder itself. Further, it peaks in brightness near the outer edge of the cylinder, strongly indiciating this is an artifact in the integration and can safely be ignored. Explain.

Still looking down-the-barrel at $t = 10.1\ Myr$, we see that the interior of the collision region has highly magnetized regions forming too, again coinciding with the formation of dense structures there. Interestingly, we also see growing voids in P_{mag} as well, marked by a decrease in β^{-1} from its initial value, $\beta^{-1} = 0.1$. These voids (shown in the lowest color on the color bar) are formed as the field is removed from these regions as it is being dragged down into the dense gas. These pockets therefore exist in-between regions of high β^{-1} in the collision region, as well as between the collision region and the outer ring.

As time goes on, there is an increase in the size of the voids as well as the islands of high β^{-1}. This indicates a large saturation in the magnitudes of β^{-1} in these regions, and at its highest, β^{-1} is many times its initial value. There are large ramifications for the ever growing regions of high β^{-1} already alluded to in Section 4 – a large scale support against gravitational collapse, which is further evidenced by the positions of newly formed protoclusters in the present column β^{-1} maps. As seen in the $t = 20.1$ and 27.3 Myr panels, protoclusters are forming away from the highest β^{-1} regions, in regions where the gas is dense enough, but $\beta^{-1} < 0.6$. A cursory glance at the right-hand panel of Fig. 6 at $t = 27.3\ Myr$ might suggest the opposite is true, however, the average β^{-1} along this line of sight is picking up the large ring structures themselves. A look at the left hand panel shows that no protoclusters have formed in the ring, and that there are large islands of saturated β^{-1} there.

6.2 $\theta = 15^\circ$ case

The column β^{-1} maps of the $\theta = 15^\circ$ case (Fig. 7) are very similar to the head-on case. Like the $\theta = 0^\circ$ case, regions of high β^{-1} are associated with the ring structure as well as dense structures that are forming in the flows. There is also the same build up of voids – regions driven by a diminished magnetic field density as described previously.

The slight shear angle does leave a small signature in the column β^{-1} maps early on, however. Looking down the barrel, at $t = 10.1\ Myr$, it is evident that there are weaker regions of enhanced β^{-1}. This is because incoming flows are dispersed from the collision region easier than in the head-on case, at least early on, and is envisioned as follows. Given the tilted interface, there is now an asymmetry in the potential flow path when incoming material meets the interface. Whereas before the material was splashed away from the collision region with radial symmetry, now material is splashed obliquely tracing the collision interface. That is, material coming into the collision region is now met with a 'ramp', either upwards or downwards facing depending on the side of the interface the flow is coming from. This means that material in projection will be elongated due to the 'ramps' (Fig.7, left, $t = 10.1\ Myr$). It also means that the magnetic field is less deformed than in the head-on case – material runs into less field lines per unit time when it is jetted away from the collision region at an angle $\theta > 0$.

Less magnetic field pressure is thus generated to retain the outgoing material. This makes for less dense structures forming in the collision region. Less dense structures correlates with less β^{-1}, as discussed above and as seen in the the present maps. By $t = 20.1\ Myr$ this effect seems to level off: regions of high n, β^{-1} more readily resemble the maps of the $\theta = 0^\circ$ case. Protoclusters that can be seen on the maps at $t = 20.1$ and 27.3 Myr also are shown to be forming in *dense enough* regions that are not at peak β^{-1} as discussed in the previous section.

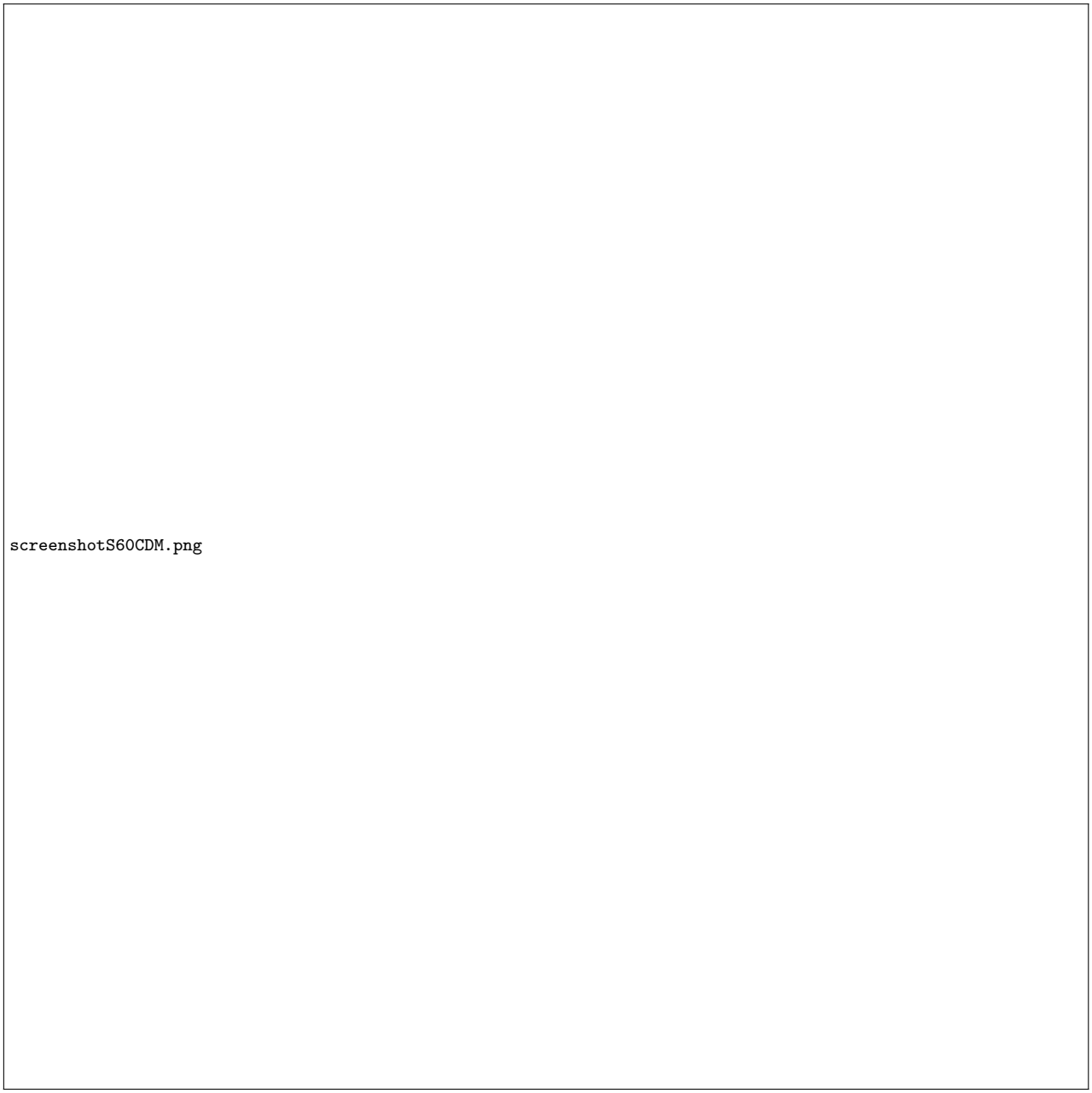

Figure 5. CDM of Shear 60

6.3 θ= 60° case

A look at Fig. 8 shows a very different set of column β^{-1} maps for the $\theta = 60°$ case. Most notably, we can see an elongated, low β^{-1} collision region looking down the barrel, and a compressed, significantly higher β^{-1} collision region when seen from the side (Fig. 8, right). The generation of such a low density and hence low β^{-1} collision region in the yz plane is understood in the framework described previously: the (now very) steep collision interface creates a ramp for incoming material to be deflected off of. Since it is traveling obliquely with respect to the field, it can travel further than when it is running into the field perpendicularly. This allows material to escape the collision region easier, resulting in a lower density and correspondigly lower β^{-1} collision region.

In contrast, the side-view at right (Fig. 8) shows a high β^{-1}. This is, however, simply due to projection effects. Given the collision region is so thin in this case, it lies within a thin cylinder through which we are integrating – resulting in a higher average β^{-1} when seen from this perspective. Over time, i.e. from $t = 20.1\ Myr$ onward, as the collision region reorients (see Section 5.3 for description), more material is getting trapped inside of the collision region. This explains the growing regions of high β^{-1} seen in the left hand side of Fig. 8. This corresponds to higher β^{-1} in the other perspective as well. By $t = 27.3\ Myr$, the right hand panel shows the collision region is beginning to stretch out in the x-direction. This makes for a now decreasing β^{-1} in the collision region in this perspective, as well as in the next time panel. All the while, more material continues to accumulate

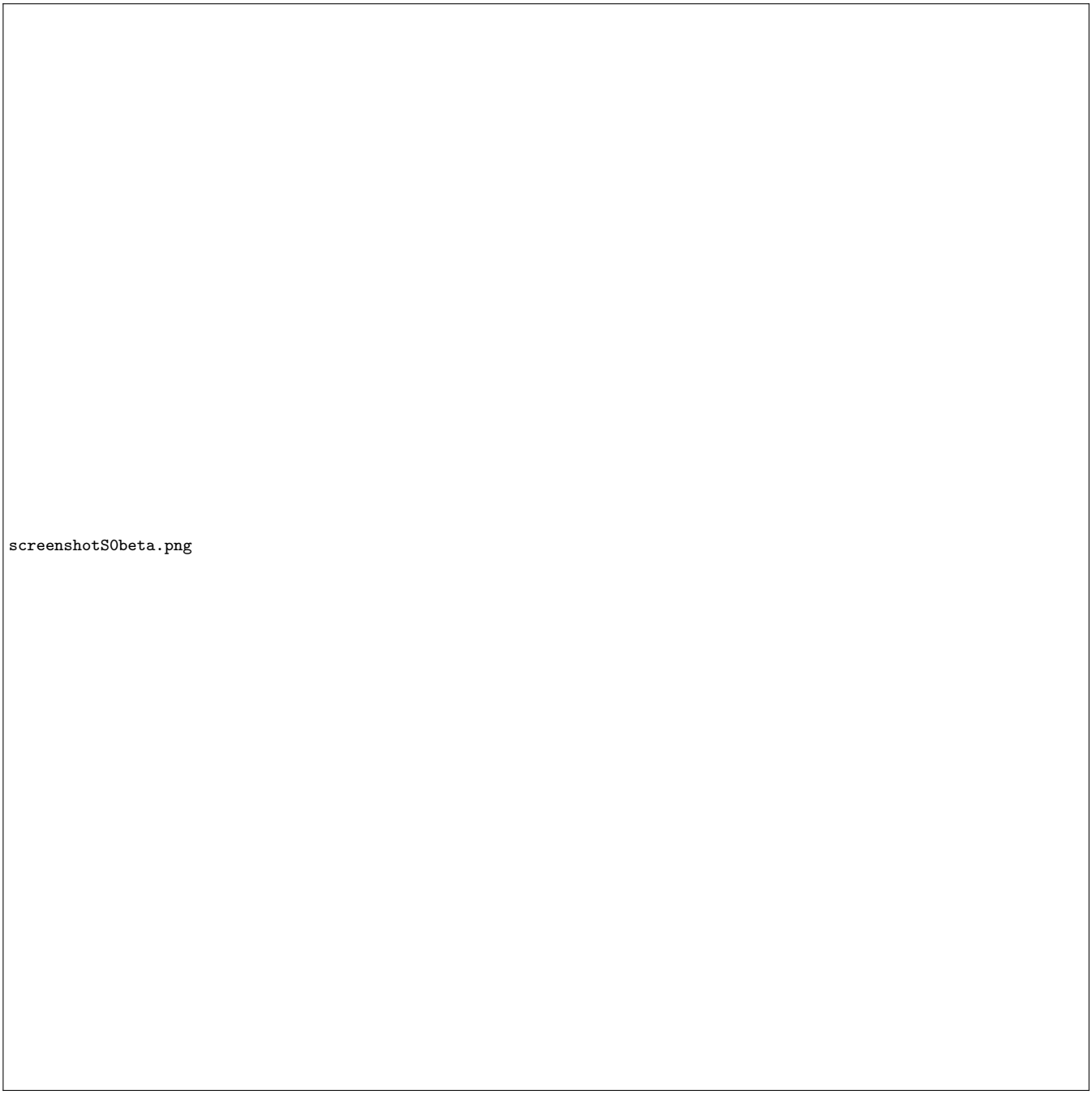

Figure 6. β^{-1} for Shear 0

in the collision region when seen in the yz plane resulting in growing β^{-1} there.

Perhaps most interesting is the position of the lone protocluster that forms in this simulation in column β^{-1} space. As can be seen in the $t = 32.8\ Myr$ panel looking down the barrel, the sink has formed again in a region of fairly low β^{-1}, close to its initial value when seen in this perspective.

7 THERMODYNAMICS - PROBABILITY DISTRIBUTION FUNCTIONS

The main thermodynamic features of the flow are commonly represented in a probability distribution function (pdf). The pdfs in this section give the mass fraction of the gas at a given pressure and number density. In our plots, the y-axis gives both scaled magnetic *and* thermal pressure (marked by the color and gray scale, respectively), and the x-axis gives number density $n(cm^{-3})$. Isotherms are straight lines of slope $m = 1$ on these pdf log-log plots, and increase in temperature from right to left.

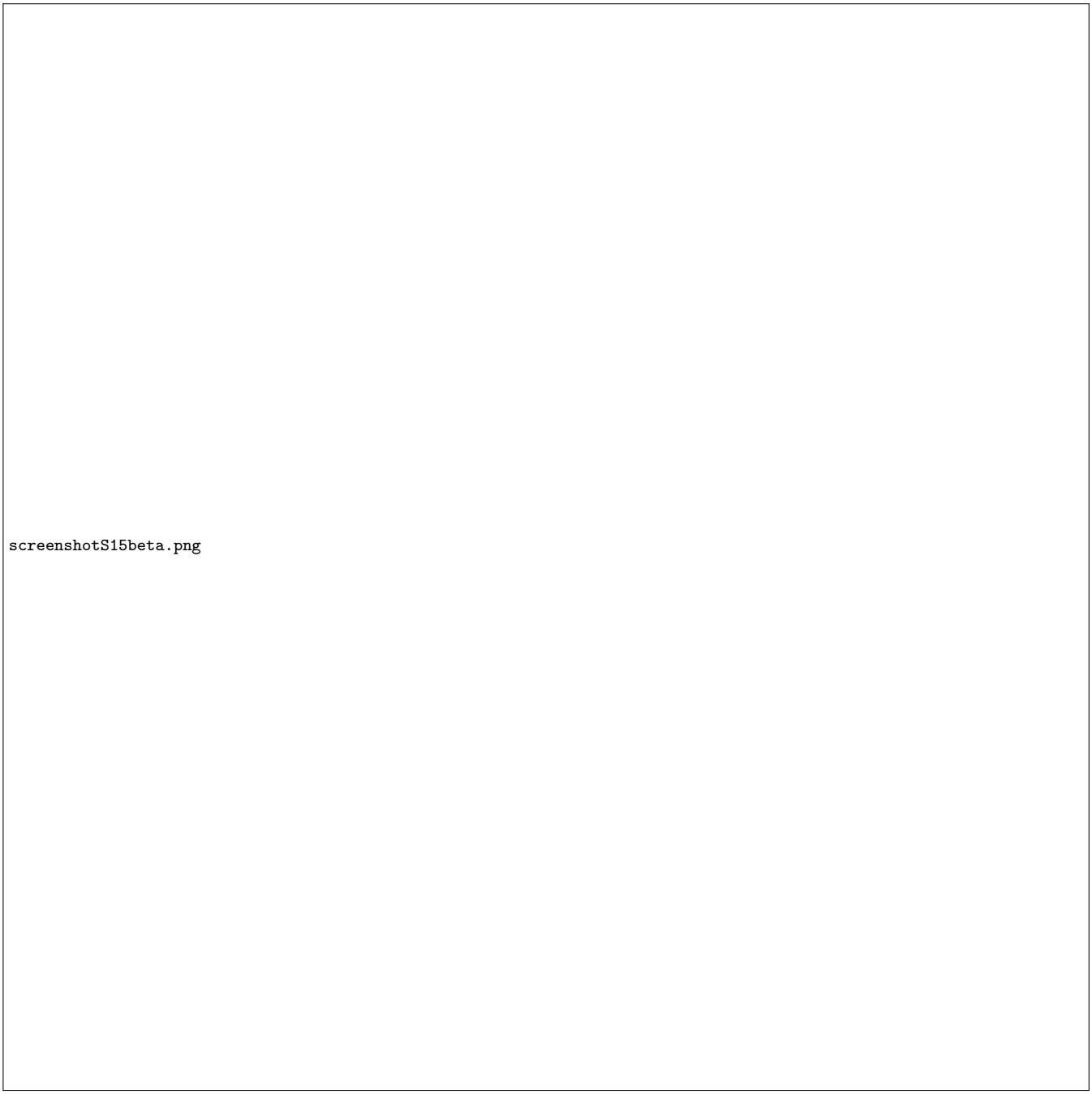

Figure 7. β^{-1} map for Shear 15

7.1 θ= 0° case

As an orientation to these plots, note the large mass fraction of gas at the initial density ($\log n = 0$) in both color and gray space in Fig. 9. Both of these populations are the original, unshocked, incoming material, and therefore have a 1-1 correlation. This is confirmed by comparing the pressures of these populations, showing $\beta = 10$ as initialized. Making such correlations between other populations in this plot is difficult, at least until above $n \approx$ 1000 cm^{-3}, when most of the gas begins to line up on the cooling curve in the $P_{therm} - n$ space, due to the extremely short cooling times out in this region (cite). Out there, the range of P_{mag} for a given n correlates to 1 population of P_{therm}, that which is constrained to lie on the equilibrium curve at that given n.

It is also important to recall the temperature read off of the isotherms only relates to the thermal pressure distribution, because $Pk_B^{-1} = nT$. If we can relate populations in the different plots, then we could get temperature information for the $P_{mag} - n$ plot as well. For example, the initial P_{mag} population is at $T \approx 4000K$ (mapping from P_{mag} space to P_{therm} space, and then checking the isotherm that runs through this region). As stated above, after about $\log n = 2.5$, we can constrain the thermal pressure of the $P_{mag} - n$ distribution since the majority of mass

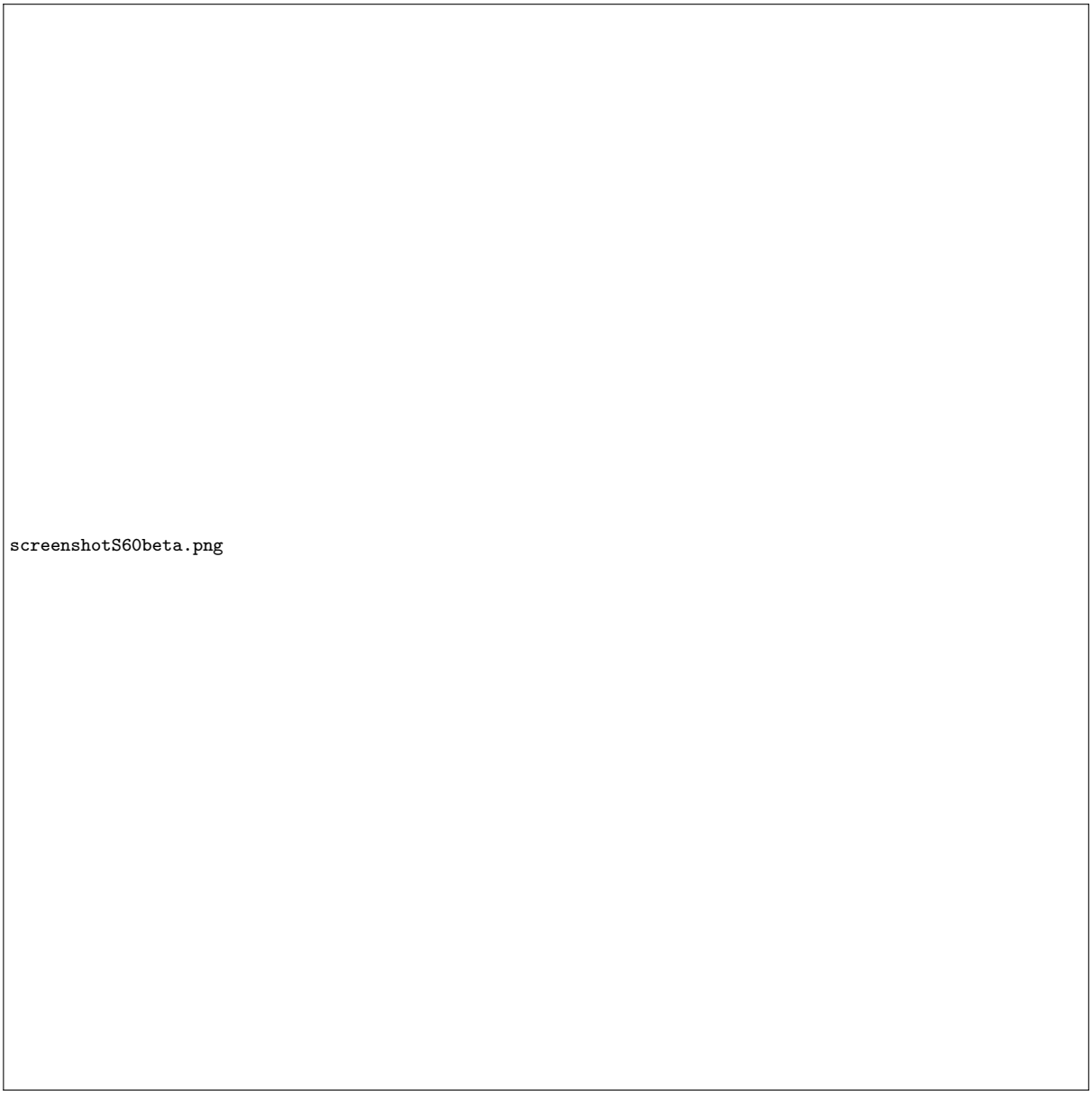

Figure 8. β^{-1} map for Shear 60

in $P_{therm} - n$ space now lies on the equilibrium curve. This means 2 things. First, above that density, we can easily identify regions above and below the equilibrium curve in $P_{mag} - n$ space as having either $\beta > 1$ (below the curve), or $\beta < 1$ (above the curve) (because we know precisely the thermal pressure of the cells with those densities), and second, we know the temperature of that dense gas is 10 K, even though there is a large spread in magnetic pressure of that gas.

Now, the thermodynamics of the flow goes as follows. Incoming material is shocked and compressed when it collides with the opposing flow, leading to higher thermal pressures, temperatures, and densities. This results in a population of gas that is above and to the right from the initial values in gray space, seen in all time states of Fig. 9. The higher density of this shocked material leads to cooling, condensing the gas so that it begins to move down and toward the right, approaching the equilibrium curve. Further cooling and condensing happens until the cooling timescale becomes so short (eventually less than a timestep of the code) that material begins to pile up on the equilibrium curve at high densities. That is to say, any process that would move gas off of the equilibrium curve would have a timescale longer than the cooling time, and so material would ultimately remain on the equilibrium curve. As time goes on, more and more gas piles up along the equilibrium curve toward higher and higher densities. Eventually the thermal pressure of this gas exceeds the ram pressure of the flows, and we attribute this to self-gravity taking its hold of the gas. At this point, sink particles *can* form.

Looking in color space now shows that the dynamics of $P_{mag} - n$ space is different. Since the shocks are not fully plane parallel (and even less so in the $\theta > 0^{\circ}$ runs), dissipation of kinetic energy is inefficient, leading to a highly

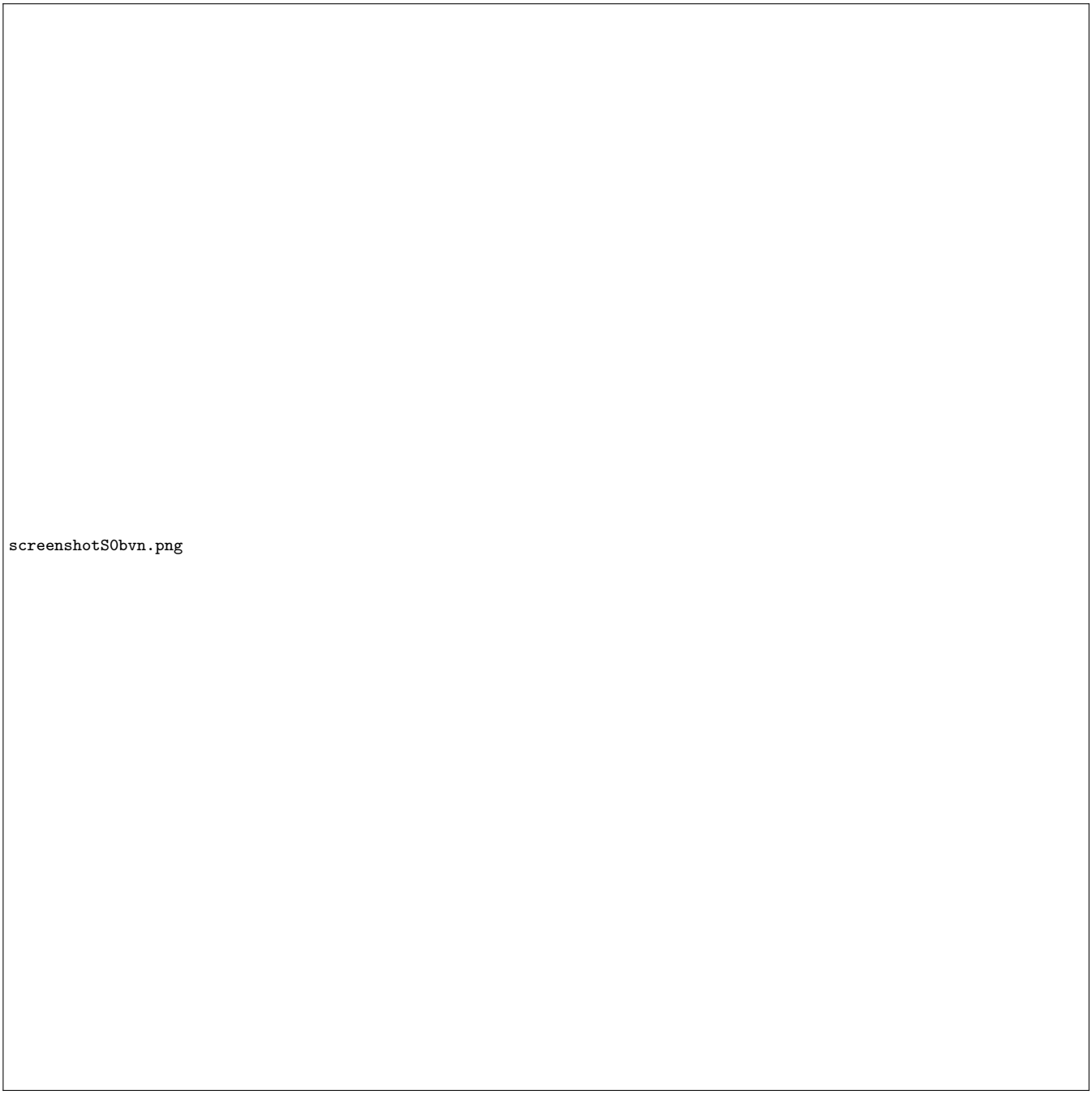

Figure 9. PDFs for Shear 0

turbulent flow. This turbulent nature of the flows explains the large spread in the $P_{mag} - n$ pdfs; in $P_{therm} - n$ space there are physical mechanisms (thermal instability, for one) that dissipate energy in the gas, while there are none in $P_{mag} - n$ space.

The majority of the mass, however, populates 2 regions of the $P_{mag} - n$ pdfs, marked in red. These are the initial values discussed above, and the rather large island above and to the right of that. Note, the color scale is a log scale, so these changes in color are significant. The upper-right island is material that was shocked and compressed to higher densities and magnetic pressures. This increased magnetic pressure is due to flux freezing accompanied by the compression. After a certain density, this island is entirely above the $P_{therm} - n$ pdf, meaning this material has a $\beta < 1$. The relatively strong field in this population can explain the lesser degree of gravitational collapse of this run compared to the hydro analog: a great deal of material has enhanced support (thermal + magnetic pressure support) in this MHD run relative to the hydro run.

Another important feature of the $P_{mag} - n$ plot is the high P_{mag}, n tail of the pdf. This tail traces the growing tail of the $P_{therm} - n$ gas, which grows along the equilibrium curve, and thus is a marker of whether self-gravity has be-

come dominant on some size scale. That is, this tail is only present in the $t > 20.1\ Myr$ panels of Fig. 9, after which protoclusters have formed. The spread in β of this tail is high, indicating that material that is *dense enough* to form protoclusters (i.e. the material which has pressures above the ram pressure of the flow as discussed above) has varying degrees of magnetic support, and the large fraction of material in this tail above the equilibrium curve (i.e. $\beta > 1$) is undoughtedly responsible for the reduced protocluster formation in the MHD run compared to the hydro run.

Finally, while the relative importance of gravity and magnetic field support is an important question to ask, the answer cannot come from this plot alone. To quantify this, one would need to correlate the mass fraction in these pdfs spatially, or in other words, back out the size scale of these populations. Similarly, one could track and analyze the cores and filaments that form in these simulations themselves as being super or sub-critical. Here, however, we can only note there is a large mass fraction with a low β that is likely correlated spatially in the grid. Such a population would have enhanced support against collapse, explaining the reduction of protocluster formation in the MHD run compared to the hydro run.

7.2 θ= 15°

The pdfs for the $\theta = 15°$ case were very similar to the $\theta = 0°$ case. The largest difference between these runs was the delay in growth of the high P_{mag}, n tail in the higher shear run. This indicates that shear suppresses compression in the flows; the higher vorticity generated by the shear provides support against self-gravity in the gas, which delays the formation of dense, high magnetic pressure populations in the flows. However, eventually enough material is collected into the collision region to outbalance the support, and the tail is seen by $t = 20.1\ Myr$, again coinciding with the presence of protoclusters in the flow.

7.3 θ= 60°

Keeping in mind the trends discussed previously, a look at Fig. 11 shows an even further delay in collapse/compression in the highest shear angle case, $\theta = 60°$. This is evident early on at $t = 10.1\ Myr$ as a diminished upper-right island of high P_{mag}, n material, indicating a lesser degree of compression in the flows. As time goes on, a reduction in the high P_{mag}, n tail is also visible at $t = 20.1\ Myr$ compared to the lower shear angle runs. In fact, this tail is still not present by $t = 27.3\ Myr$, indicating a lack of high density material being generated in the flows. This is not surprising, given no protoclusters have formed in the flow by this time. The dynamics of the flows, as evident by the pdfs, are so similar between the 2 time states $t = 20.1$ and $27.3\ Myr$ that we have left out the later time state from the plot. We attribute this mostly to the greater support afforded to the gas by the high shear of the flows, which slows down its evolution. (<-Perhaps a clearer way of saying this.)

By $t = 32.8\ Myr$, a high P_{mag}, n tail is now present in the pdf, coinciding of course with the presence of a newly formed protocluster in the flow. It is interesting to note that while this tail has a range of magnetic pressures, all of the gas occupying the tail has a $\beta < 1$. This contrasts with the other cases, where material in the tail varied as $|\beta| > 1$.

Table 2. Spectra region for the different runs, with accompanying minimum wave number k_{min}.

$\theta(°)$	$L_x\ (pc)$	$L_y,\ L_z\ (pc)$	λ_{max} (pc)
0	20	40	40
15	31	40	40
60	90	40	90

At first glance, this feature could indicate 1 of 2 things. Either, early on in the development of the tail (i.e. during the formation of dense structures in the gas), the gas does not have time enough to relax from the high P_{mag} state imparted to the gas due to flux freezing. That is, all of the simulations might pass through this phase of a low β tail – i.e. only once enough time has passed for excess P_{mag} to be removed from the gas can a spread in β manifest in the tail. The $\theta = 60°$ case being slower to evolve, would thus have to evolve further into this state.

This situation however is unlikely, given the lack of ambipolar diffusion in the present suite of simulations. Such a reduction of P_{mag} in the gas, without a concomitant decrease in n would only be possible due to magnetic reconnection in the gas, more likely to occur in the most severely distorting magnetic field case, which is presumably the present $\theta = 60°$ run. The high distortions in the field are possible in this run given the sharp deflection of the gas at the highly oblique boundary between the flows. On the largest scales, each side of the boundary is being deflected away in opposite directions, leading to a high degree of kinking in the magnetic field. This kinking has the potential of bringing oppositely directed field close together, leading to extrememly large magnetic pressures and a tendancy for the field to reconnect.

This then suggests the 2nd possibility – this low β tail is a prominent feature in the $\theta = 60°$ case only. It is created due to the large distortions in the field being generated by the deflection of the flow from the collision interface, making for high P_{mag} in the high n material. The excess of high P_{mag} in this population must make it extremely difficult to form protoclusters in such an environment; the single protocluster that has formed, has done so despite having strong support against collapse.

8 ENERGY ANALYSIS - SPECTRA

Spectra were made following Carroll-Nellenback, Frank & Heitsch (2014). To accomodate the steeper shear angle, the regions over which the spectra were taken changed for each of the runs, as given in Table 2. Each of the spectra regions added a $\Delta x = 10\ pc$ to each side of the collision region, whose width we define as $x = 40 \tan\theta\ (pc)$. Note, the $\hat{x}$-axes in the spectra are equivalent to $\lambda_{max}\lambda^{-1}$.

8.1 θ= 0°

Spectra for the $\theta = 0°$ case are given in Fig. 12 for 3 different time states, $t = 10.1$, 20.1, and $27.3\ Myr$. In the $t = 10.1\ Myr$ panel of these (and all subsequent spectra),

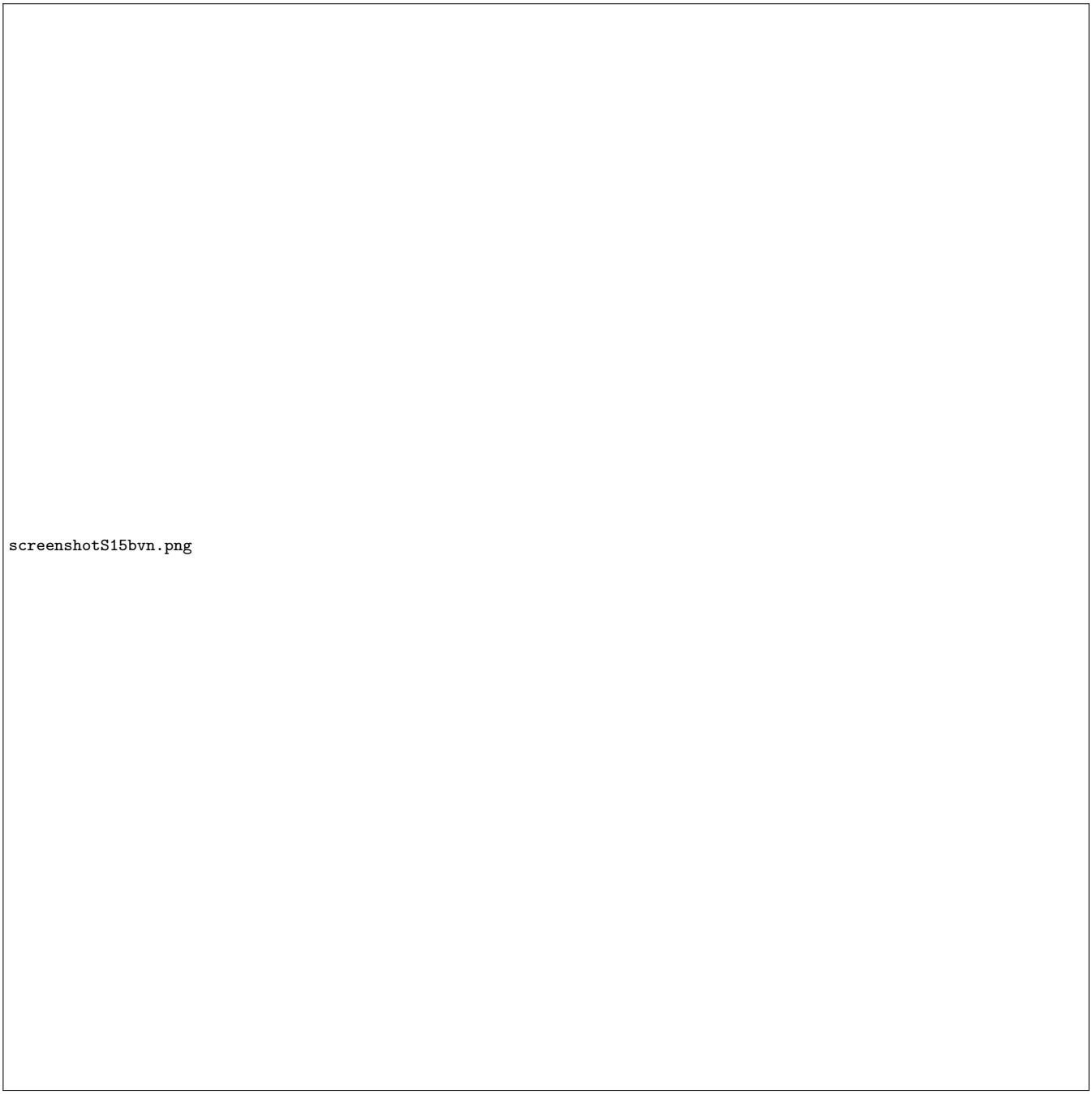

Figure 10. PDF for Shear 15

we include a k^{-2} line to compare to the spectra of v^2, in addition to spectra for magnetic (E_{mag}), gravitational (E_{grav}), and kinetic (E_{kin}) energies. At later times, we do not include these curves, as they are largely unchanged throughout the other time panels of the figure.

As can be seen in the $t = 10.1\ Myr$ panel, gas at scales above $kk_{min}^{-1} = 20$ and below $kk_{min}^{-1} = 9$, is far away from a burger's type turbulent spectrum ($v^2 \propto k^{-2}$). At intermediate scales, however, the v^2 spectrum is nearly parallel to the k^{-2} line. Explain.

The dominant energy on all size scales in this time state, as well as all other times, is E_{kin}. This is due to the overwhelming power being generated in the colliding flows themselves. Explain. Interestingly on the smallest scales, magnetic energy surpasses gravitational energy, and approaches the kinetic energy spectrum. This scale corresponds to ($\lambda \approx .1\ pc$), the Nyquist frequency for these spectra, above which we can no longer plot spectrum with confidence.

Continuing to look at the $t = 10.1\ Myr$ panel, we see that E_{grav} dominants E_{mag} on most other size scales. The interesting exception is the same intermediate region discussed above. That is, for $9 < kk_{min}^{-1} < 20$, we see that E_{mag} is comparable to E_{grav}. Note, this corresponds to size

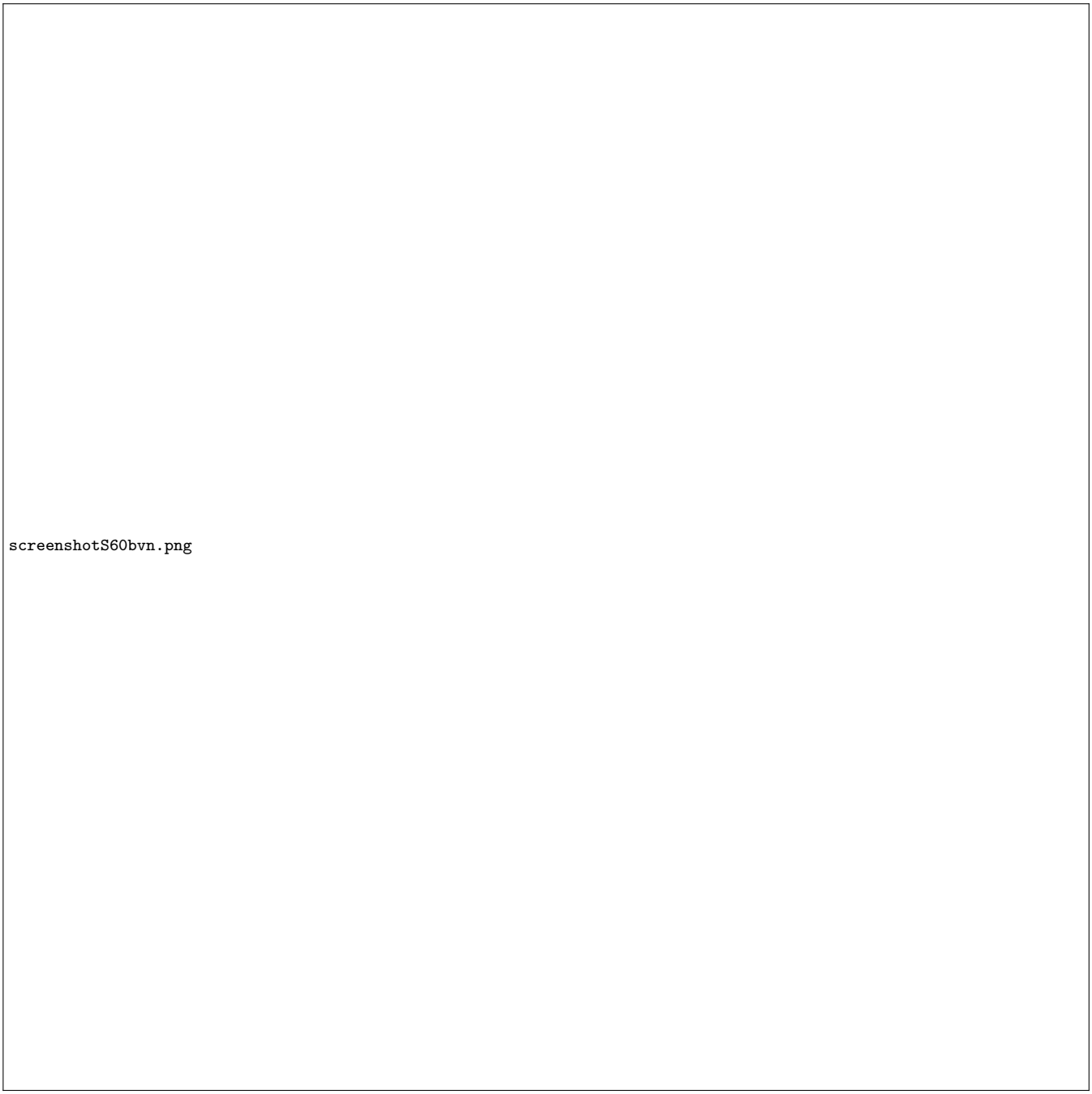

Figure 11. PDFs of Shear 60

scales $2 < \lambda\ (pc) < 4$. Explain what is going on in the flows on these size scales.

By $t = 20.1\ Myr$, not much changes in the spectra. Explain why. However, by $t = 27.3\ Myr$, we see an increase in E_{mag} for size scales again between $2 < \lambda\ (pc) < 4$, making E_{mag} dominant over gravitational energy. Magnetic energy continues to dominate over gravitational energy on the smallest scales as well, indicating a lack of local gravitational collapse.

8.2 θ= 15°

This case shows the same behavior as the $\theta = 0°$ case, but now we are not showing an increase of magnetic energy *over* gravitational energy on the intermediate scales. Why.

8.3 θ= 60°

The spectra for the $\theta = 60°$ case is different than the previous 2 cases, it shows that the magnetic energy is dominant over the gravitational energy on all size scales, and approaches the kinetic energy spectrum in the range of $10 < kk_{min}^{-1} < 100$ corresponding now to size scales be-

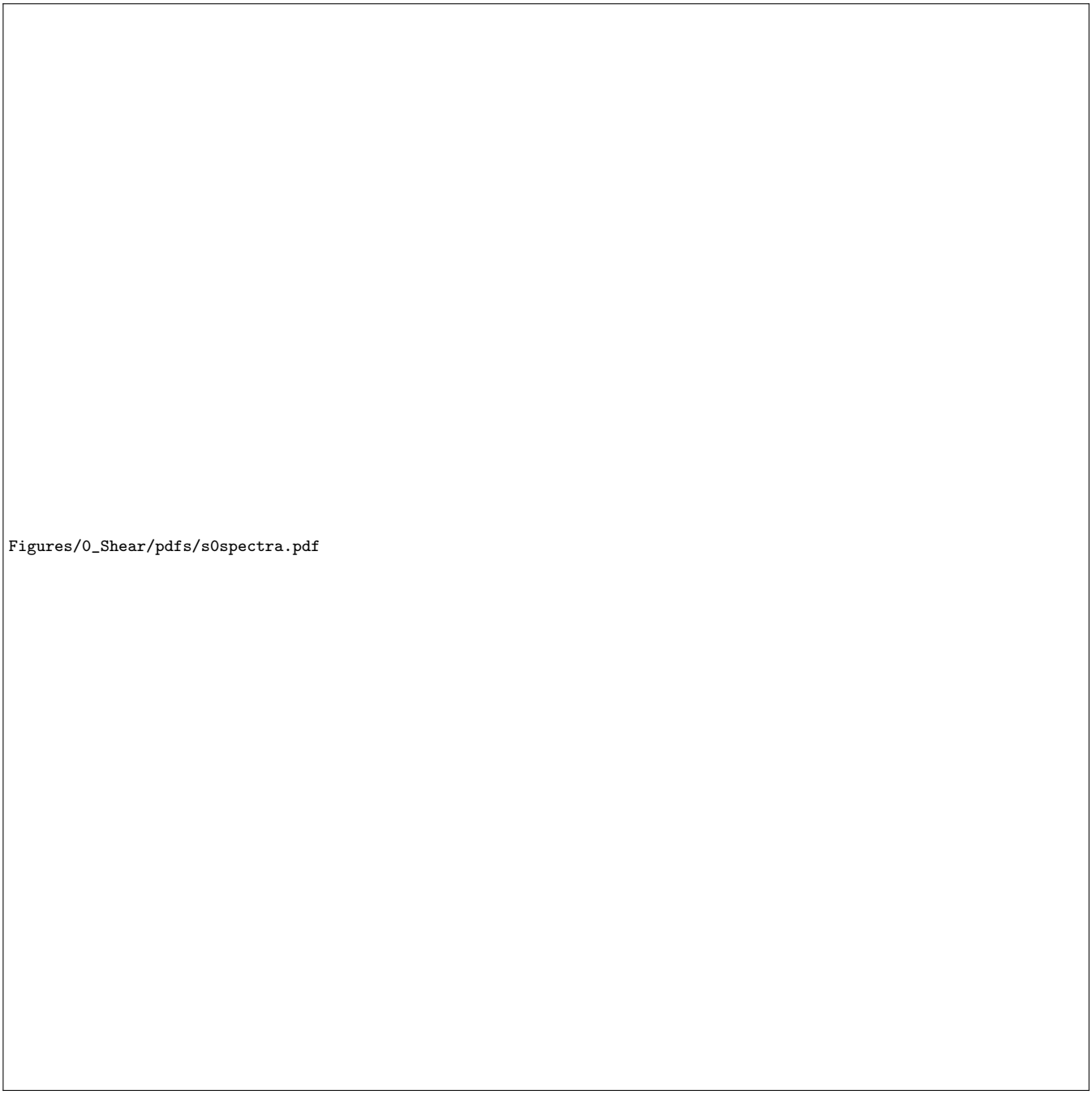

Figure 12. Spectra for Shear 0

tween $0.9 < \lambda(pc) < 90$. Note, the Nyquist frequency is now pushed to the right in this plot, as the spectra region now has a different k_{min} (cf. Table 2). Over time ($t = 20.1$ to 27.1 Myr), gravitational energy approaches magnetic energy on the largest scales (90 pc to about 10 pc). Note, the $t = 27.3$ Myr panel is not shown here, as it does not significantly differ from the $t = 20.1$ Myr panel. By $t = 32.8$ Myr, we have again added the v^2 and k^{-2} line, as it has begun to approach a Burger's type turbulent spectrum, for $kk_{min}^{-1} < 100$. The gas is mainly magnetically supported on all size scales by this time still, however, as gravitational energy spectrum just begins to overide the magnetic spectrum for given k.

9 SUMMARY

We have presented 3-dimensional, adaptive mesh refinement simulations of magnetized colliding flows using the ideal magnetohydrodynamics code, AstroBEAR, including self-gravity, sink particles, and cooling. Feedback was not included in the present work. These simulations were of 2 colliding flows, intersecting at a tilted collision interface under a dynamically weak magnetic field. The degree of tilt in the

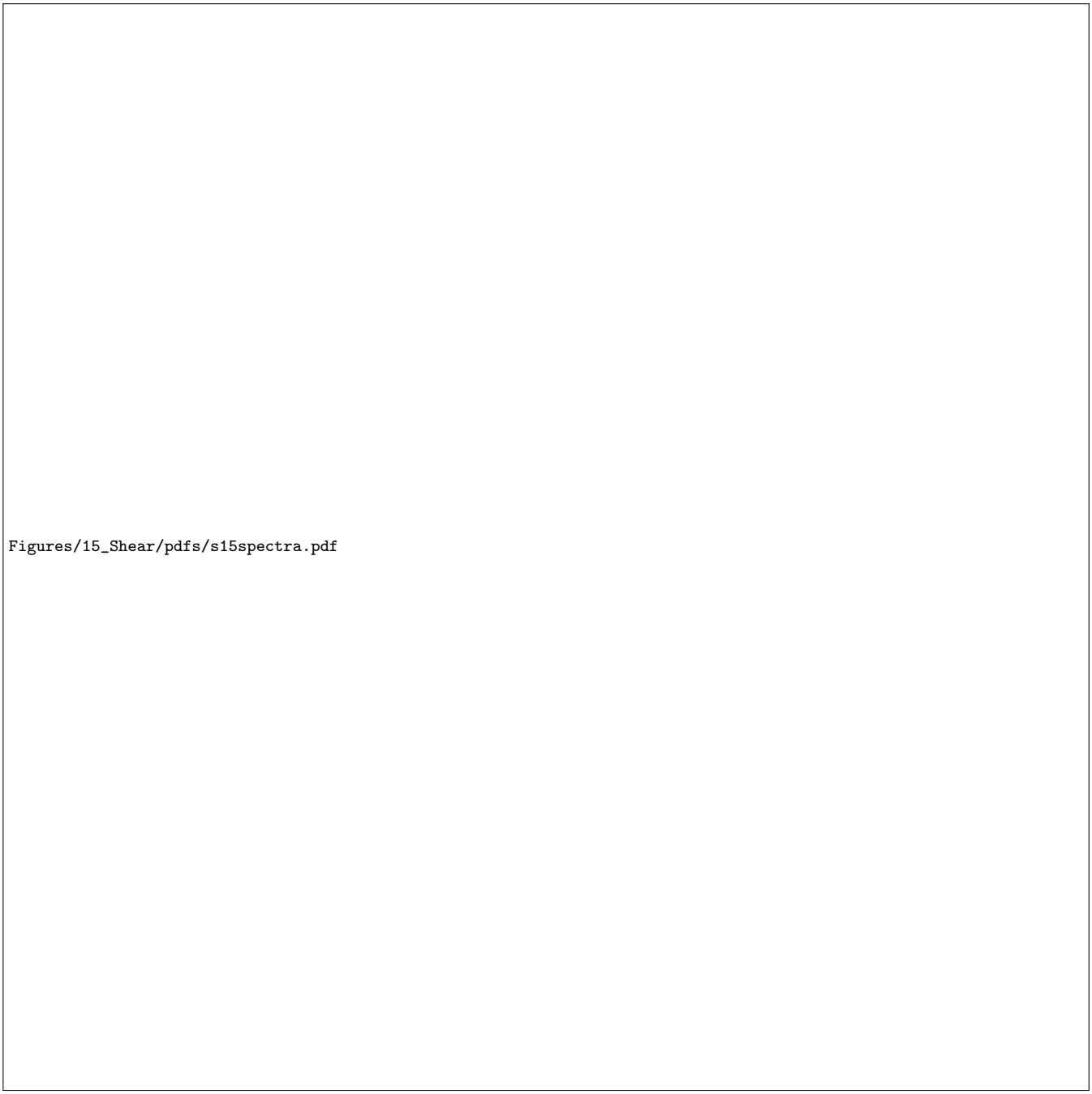

Figure 13. Spectra for Shear 15

collision interface was varied to study the effect of shear on the resultant gas dynamics in the collision region.

Our main conclusions are summarized as follows:

(i) Magnetic fields inhibit sink particle formation in a head-on colliding flows scenario. This has been found in various other simulations of colliding flows (cite), as well as in simulations of turbulent cluster formation (cite).

(ii) The initial conditions of the collision interface are erased after large scale gravitational collapse sets in (evidenced by cloud morphology and realligning of the collision interface).

(iii) The transition from WNM to CNM is delayed in high shear environments.

(iv) Dense structures form later, and don't get as dense in high shear environments.

(v) Higher shear impedes gravitational collapse.

ACKNOWLEDGMENTS

We would like to thank Rich Sarkis of the University of Rochester for his help with data management, the University of Rochester's Center for Integrated Research Computing for time on their supercomputer machines, data stor-

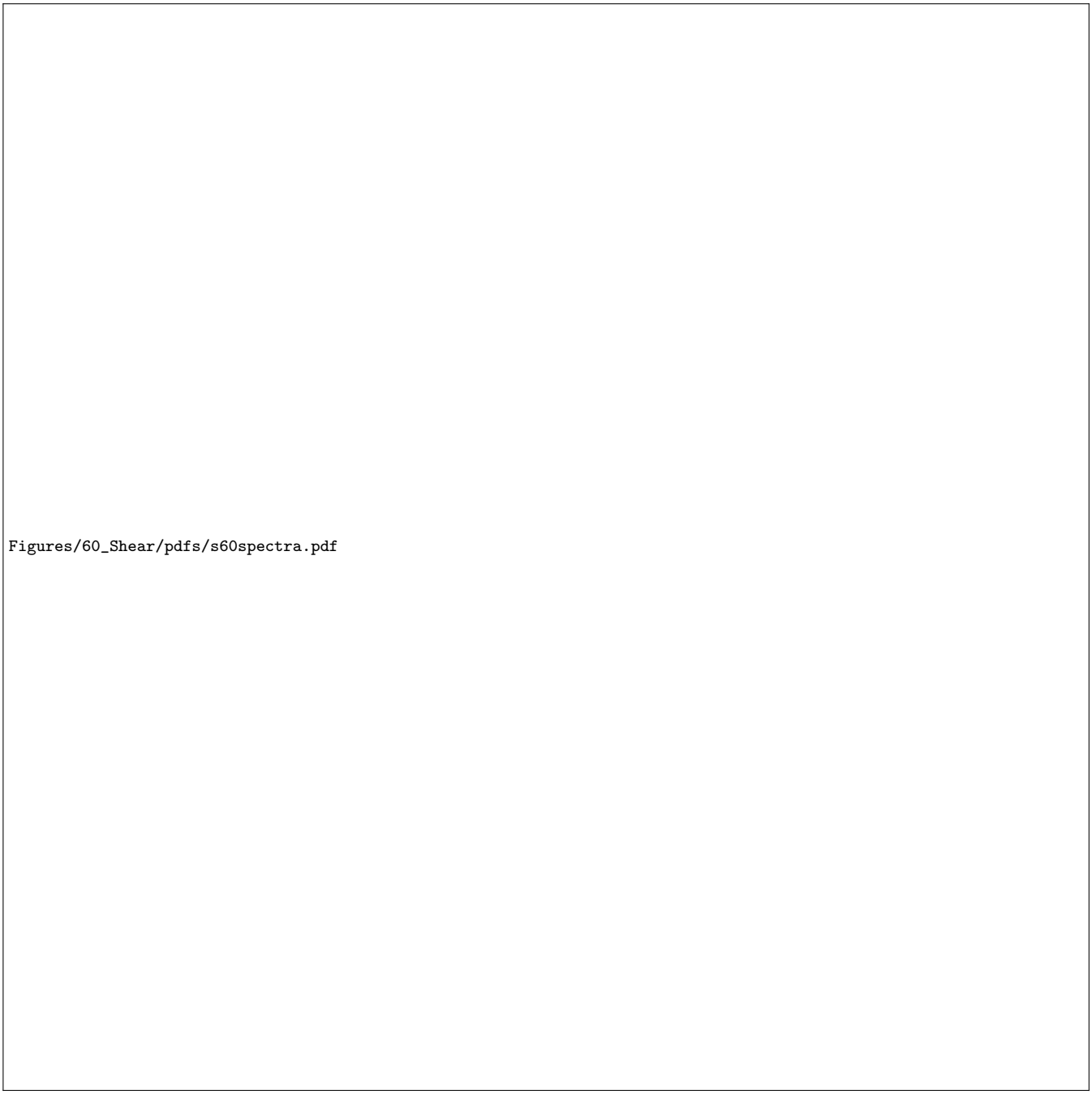

Figure 14. Spectra for Shear 60

age, and visualization at the VISTA collaboratory, and the Texas Advanced Computing Center and XSEDE for computing time. We would also like to thank the National Science Foundation for supporting this research through grant X.

REFERENCES

Alves F. O., Franco G. A. P., Girart J. M., 2008, A&A, 486, L13

Audit E., Hennebelle P., 2005, A&A, 433, 1

Ballesteros-Paredes J., Hartmann L., 2007, RMxAA, 43, 123

Ballesteros-Paredes J., Hartmann L., Vázquez-Semadeni E., 1999, ApJ, 527, 285

Banerjee R., Vázquez-Semadeni E., Hennebelle P., Klessen R. S., 2009, MNRAS, 398, 1082

Beck R., 2001, SSRv, 99, 243

Brunt C. M., 2003, ApJ, 583, 280

Carroll-Nellenback J., Frank A., Heitsch F., 2014, ApJ, 790, 37

Carroll-Nellenback J. J., Shroyer B., Frank A., Ding C., 2013, Journal of Computational Physics, 236, 461

Crutcher R. M., 1999, ApJ, 520, 706
Crutcher R. M., Wandelt B., Heiles C., Falgarone E., Troland T. H., 2010, ApJ, 725, 466
Dawson J. R., McClure-Griffiths N. M., Dickey J. M., Fukui Y., 2011, ApJ, 741, 85
Dawson J. R., McClure-Griffiths W. T., Dickey J. M., Hughes A., Kawamura A., 2013, ApJ, 763, 56
Elmegreen B. G., 2000, ApJ, 530, 277
Falgout R., Yang U., 2002, j-lect-notes-comp-sci, 2331
Federrath C., Banerjee R., Clark P. C., Klessen R. S., 2010, ApJ, 713, 269
Hartmann L., 2001, AJ, 121, 1030
Hartmann L., Ballesteros-Paredes J., E. B., 2001, ApJ, 562, 852
Heitsch F., Burkert A., Hartmann L., Slyz A. D., Devriendt J. G., 2005, ApJ, 633, L113
Heitsch F., Hartmann L. W., Slyz A. D., Devriendt J. E. G., Burkert A., 2008, ApJ, 674, 316
Heitsch F., Slyz A. D., Devriendt J. E. G., Hartmann L. W., Burkert A., 2006, ApJ, 648, 1052
Heitsch F., Slyz A. D., Devriendt J. E. G., Hartmann L. W., Burkert A., 2007, ApJ, 665, 445
Heitsch F., Stone J. M., Hartmann L. W., 2009, ApJ, 695, 248
Hennebelle P., Banerjee R., Vázquez-Semadeni E., Klessen R. S., Audit E., 2008, A&A, 486, L43
Hunter J. H., 1979, ApJ, 233, 946
Hunter J. H., Sandford II M. T., Whitaker R. W., Klein R. I., 1986, ApJ, 305, 309
Inutsuka S., Inoue T., Iwasaki K., Hosokawa T., 2015, A&A, forthcoming
Kaminski E., Frank A., Carroll J., Myers P., 2014, ApJ, 790, 70
Körtgen B., Banerjee R., 2015, MNRAS, 451, 3340
Larson R. B., 1981, MNRAS, 194, 809
Looney L. W., Wang S., Hamidouche M., Safier P. N., Klein R., 2006, ApJ, 642, 330
Palmeirim P. et al., 2013, A&A, 550, A38
Peretto N. et al., 2012, AAP, 541, A63
Sugitani K. et al., 2011, ApJ, 734, 63
Tritsis A., Panopoulou G. V., Mouschovias T. C., Tassis K., Pavlidou V., 2015, MNRAS, 451, 4384
Troland T. H., Heiles C., 1986, ApJ, 301, 339
Vázquez-Semadeni E., Banerjee R., Gómez G. C., Hennebelle P., Duffin D., Klessen R. S., 2011, MNRAS, 414, 2511
Vázquez-Semadeni E., Dongsu R., Passot T., Gonzalez R. F., Gazol A., 2006, ApJ, 643, 245

This paper has been typeset from a TEX/ LATEX file prepared by the author.